JACS
JOURNAL OF THE AMERICAN CHEMICAL SOCIETY
pubs.acs.org/JACS
Article

# Transforming 2D Imine into 3D Thiazole Covalent Organic Frameworks by Conjugated Connectors: Fully Conjugated Photocatalysts

Maojun Deng, Jeet Chakraborty, Guizhen Wang, Kuber Singh Rawat, Laurens Bourda, Jiamin Sun, Ipsita Nath, Yanwei Ji, Pieter Geiregat, Veronique Van Speybroeck, Xiao Feng,* and Pascal Van Der Voort*

Cite This: https://doi.org/10.1021/jacs.4c15825

Read Online

ACCESS | Metrics & More | Article Recommendations | Supporting Information

**ABSTRACT:** We developed a robust three-dimensional (3D) covalent organic framework (COF), fully conjugated in both the planar ($x$, $y$) and interlayer ($z$) directions, using a one-pot sulfurization process. We converted the two-dimensional (2D) imine-linked COF (Py-BDA-COF) to the 3D thiazole-linked COF (3D-Py-BDA-S-COF). In the interlayer direction ($z$-axis), the alternating covalently bound acetylene and ethylene arrangements serve as conjugated connectors ("pillars") and create a fully conjugated and very robust COF in all three dimensions. On top of this, the presence of the sulfur lone pair electrons in the thiazole rings considerably enhances the electron delocalization degree of the frameworks. The 3D-Py-BDA-S-COF is successfully evaluated in the photocatalytic reduction of nitrobenzene.

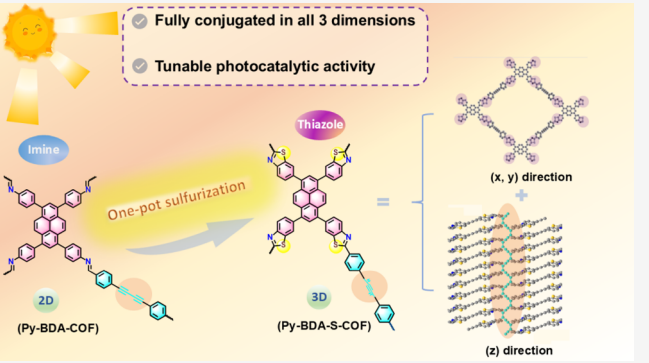


## INTRODUCTION

Fully conjugated organic macromolecules play a crucial role in advancing the fields of electronics, photonics, and energy conversion, as they enable efficient charge transport and light absorption across extended molecular systems.[1−3] Enhancing conjugation, especially in large molecules such as polymers, is particularly important because it facilitates charge carrier mobility, extends $\pi$-electron delocalization, and improves the stability of materials.[3−7]

Covalent organic frameworks (COFs) are a family of crystalline and porous polymers, with well-ordered structures, large surface areas, and customizable redox-active sites.[8] In the last two decades, extensive research on COFs has been performed in various fields such as photocatalysis,[9−11] photoluminescence,[12] optoelectronics,[13] and energy storage.[14,15] The building blocks of COFs are linked via covalent bonds to form crystalline and regular structures, which have a high degree of tunability. Typically, two-dimensional (2D) COFs have a layered stacking structure by stacking ($x$, $y$) planes, forming one-dimensional (1D) channels. Till now, the majority of 2D COFs are linked by imine bonds, as imine-COFs are relatively easy to synthesize with predictable topologies. However, the limited conjugation, poor stability, and anisotropic properties of 2D imine COFs restrict the efficient charge transport in the interlayer direction, thereby limiting their applications in photocatalysis, energy storage, and molecular electronics.[16]

Our group demonstrated in 2023 that the conversion from imine bonds to thiazole bonds enhances the planar $\pi$-conjugation, significantly boosting the photocatalytic abilities and functions (Figure 1a).[11] On the other hand, substantial efforts have been made toward the construction of three-dimensional (3D) COFs,[17−22] which offer interconnected pore channels, isotropic properties, and enhanced stability for applications such as gas separation, ion conduction, and photocatalysis.[17,23−25] In 2021, in a short communication, Feng et al. constructed 3D COFs with a conjugated bonding in the $z$-direction by solid-state topological polymerization of diacetylene units, as shown in Figure 1b.[26] Indeed, the use of cross-linking techniques to covalently connect adjacent layers is an effective strategy for creating stable, interconnected networks.[16,24,26,27] Compared with $\pi\cdots\pi$ stacking in 2D COFs, interlayer cross-linking provides a more efficient pathway for electron transport, which is potentially favorable for photo-

Received: November 8, 2024
Revised: February 7, 2025
Accepted: February 10, 2025

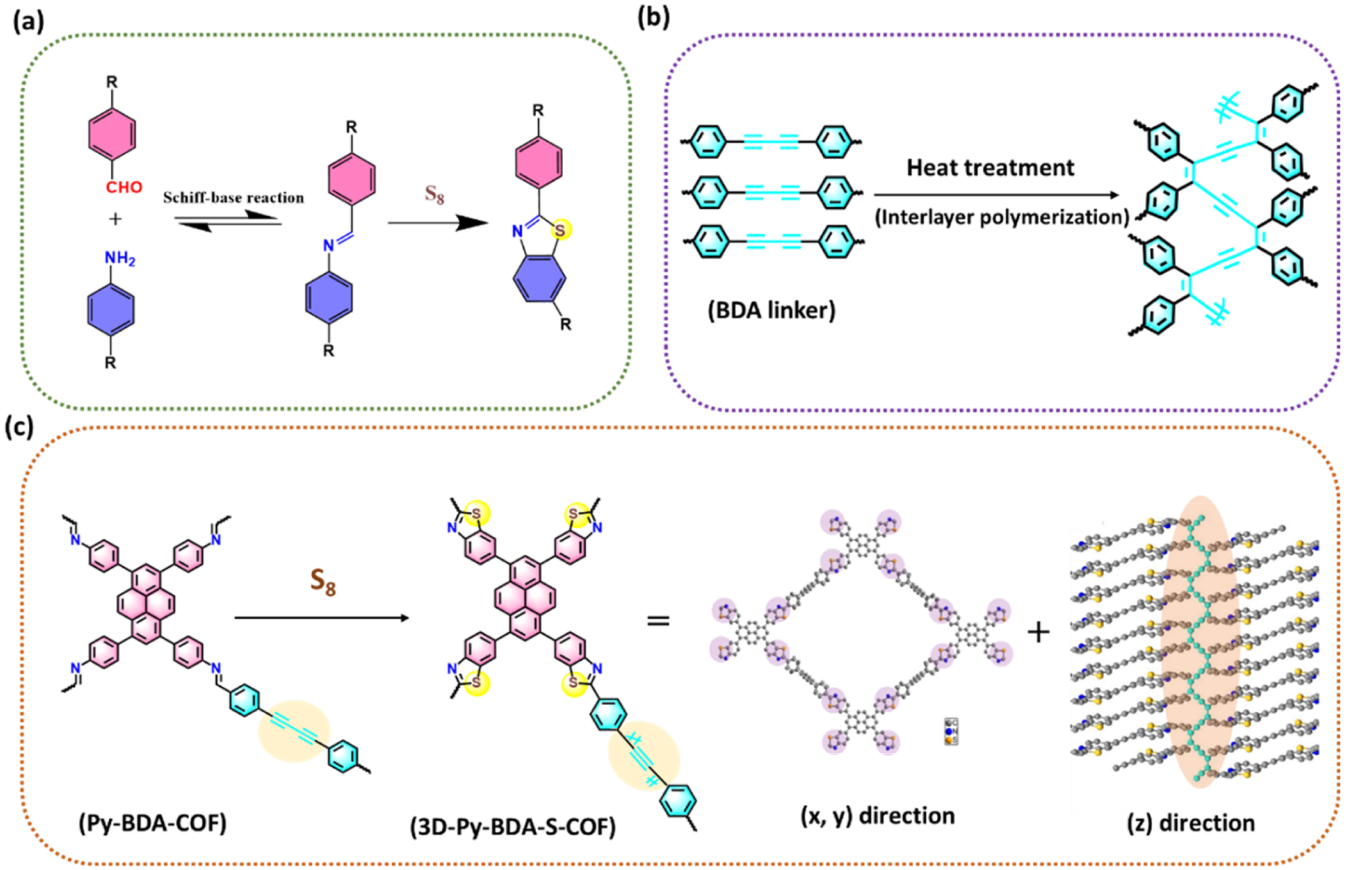


**Figure 1.** Schematic representation of (a) imine to thiazole transformation for a model compound,[11,28] (b) topochemical polymerization of diacetylene monomer,[26,29] (c) Py-BDA-COF and 3D-Py-BDA-S-COF.

catalytic reactions. Besides, it is mostly assumed that crystallinity is a critical factor for the material's photoelectronic performance, as defects and amorphous patches are regarded as charge traps. So, the challenge is the design of a photoactive COF with $\pi$-conjugation in all three dimensions, with a high degree of crystallinity and porosity.

Inspired by the above studies, in this work, we use both strategies in a one-pot sulfurization process: conjugation and stabilization of the imine bonds into thiazole bonds in the ($x$, $y$) plane and cross-linking in the $z$-direction by the polymerization of diacetylene units, hereby transforming a 2D COF into a 3D COF. In practice, we converted the 2D imine-linked Py-BDA-COF into the thiazole-linked 3D-Py-BDA-S-COF (see Figure 1c). It is important to emphasize here that the resulting material is completely conjugated in all three dimensions and has a donor−acceptor functionality, as the lone electron pair on S is an electron donor (Figure 1c). Moreover, the thiazole rings are strongly conjugated and planar by virtue of the S−C bonds. Simultaneously, conjugation in the $z$-direction is realized by the thermal polymerization of the organic ligand 4,4′-(butyl-1,3-diyne-1,4-diyl)diphenylaldehyde (BDA) during the heating process. This polymerization results in the formation of alternating arrangements of double and triple bonds, creating a highly conjugated $\pi$-electron delocalization system. This approach not only preserves the structural integrity of the framework but also allows for continuous $\pi$-electron delocalization in all three dimensions, which considerably improves the electronic properties of the material. Along this line, we anticipate that the newly formed 3D-Py-BDA-S-COF has improved photochemical features compared to the starting imine-linked COF (Py-BDA-COF), including a narrower band gap, more efficient charge separation, and a denser electron density structure. For comparison, the analogous 2D imine-linked Py-N-COF and its 2D Py−N−S-COF that underwent the same postsulfurization process were also prepared, but these materials do not go through the polymerization reaction along the $z$-axis and remain in a 2D stacked structure upon sulfurization. Our findings indicate that fully conjugated 3D-Py-BDA-S-COF exhibit the best performance among metal-free photocatalysts for the reduction of nitrobenzene.

## RESULTS AND DISCUSSION

The Py-N-COF and Py-BDA-COF were synthesized via the Schiff-base condensation of 4,4′,4″,4‴-(pyrene-1,3,6,8-tetrayl)-tetraaniline (Py-$(NH_2)_4$) and naphthalene-2,6-dicarbaldehyde (N) or BDA linkers (Figure S1). The Py−N−S-COF and 3D-Py-BDA-S-COF were prepared by subjecting the pristine Py-N-COF and Py-BDA-COF to our reported sulfurization process.[11] During the sulfurization treatment for Py-BDA-COF, the imine linkages transfer to thiazole linkages, while simultaneously, the diacetylene groups undergo polymerization in the $z$-direction, resulting in the formation of 3D-Py-BDA-S-COF. For comparison, 3D-Py-BDA-COF was developed using the same heating procedure without the addition of sulfur. In this case, only diacetylene polymerization in the interlayer direction occurs (Figure 1 and see Supporting Information for more details).

The crystalline structures of the created materials were analyzed by powder X-ray Diffraction (PXRD) and compared


https://doi.org/10.1021/jacs.4c15825
J. Am. Chem. Soc. XXXX, XXX, XXX−XXX

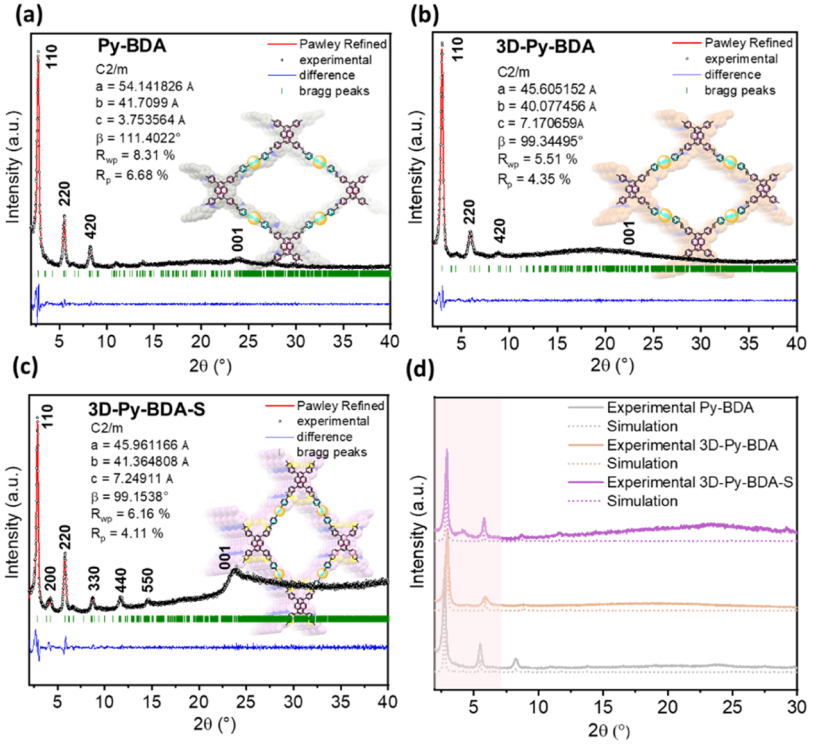


**Figure 2.** PXRD patterns and Pawley refinements of (a) Py-BDA-COF, (b) 3D-Py-BDA-COF, (c) 3D-Py-BDA-S-COF, and (d) PXRD pattern comparison of Py-BDA-COF, 3D-Py-BDA-COF, and 3D-Py-BDA-S-COF. Inset images are modeled crystal structures.

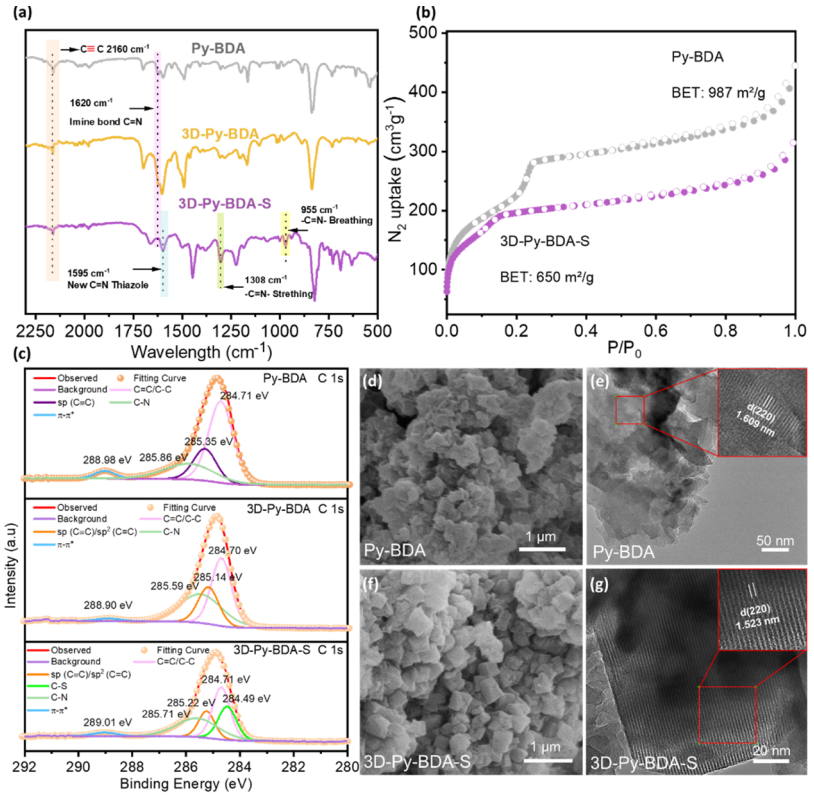


**Figure 3.** (a) FT-IR spectra of the BDA linker, Py-BDA-COF, 3D-Py-BDA-COF, and 3D-Py-BDA-S-COF. (b) $N_2$ adsorption−desorption isotherms of Py-BDA-COF and 3D-Py-BDA-S-COF. (c) X-ray photoelectron spectroscopy (XPS) high-resolution spectra of Py-BDA-COF, 3D-Py-BDA-COF, and 3D-Py-BDA-S-COF in the region of C 1s. (d−g) SEM images and TEM images of Py-BDA-COF and 3D-Py-BDA-S-COF.

to theoretical simulations. The Pawley refinement of Py-N-COF, Py−N−S-COF, Py-BDA-COF, 3D-Py-BDA-COF, and 3D-Py-BDA-S-COF was performed in the monoclinic space group *C*2/*m* on the basis of eclipsed AA stacking modes, as



https://doi.org/10.1021/jacs.4c15825
J. Am. Chem. Soc. XXXX, XXX, XXX−XXX

**Scheme 1. Synthesis Pathways of 3D-Py-BDA-S-COF via One-Pot and Two-Step Methods**

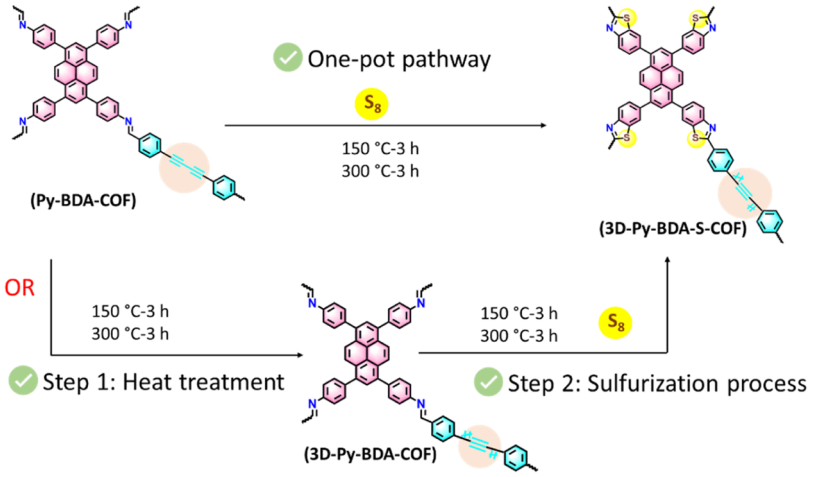


depicted in Figures 2 and S2, yielding an excellent match with the experimental pattern. The models underwent geometric optimization, followed by Pawley refinement against the experimental PXRD data. The resulting refinement parameters were as follows: Py-N-COF (Rp = 3.28%), Py−N−S-COF (Rp = 3.45%), Py-BDA-COF (Rp = 6.68%), 3D-Py-BDA-COF (Rp = 4.35%), and 3D-Py-BDA-S-COF (Rp = 4.11%). Py-N-COF and Py−N−S-COF exhibit comparable low-angle reflection peaks, while 3D-Py-BDA-COF shows a shift to higher $2\theta$ angles compared to the 2D Py-BDA-COF (Figure 2d). These shifts can be attributed to the topological polymerization of the BDA linkers, resulting in increased interlayer conjugation.[26,30] Also, these shifts were reflected in the refined unit cell parameters ($a$ = ∼39 Å for Py-N-COF and Py−N−S-COF while $a$ = ∼54 Å for Py-BDA-COF). This observation aligns with findings in earlier works as well (see Tables S1 and S2).[26,30] In parallel, the crystalline sulfur peak vanished in Py−N−S-COF and 3D-Py-BDA-S-COF experimental patterns, indicating a good integration of $S_8$ into their skeletons.[31]

Fourier transform infrared (FT-IR) measurements were performed to characterize the detailed chemical functions in the COFs (Figures 3a and S3). In acetylene-containing COFs, a distinct peak corresponding to the C≡C bond was clearly observed around 2160 $cm^{-1}$.[32−34] Additionally, a new peak emerged at 1513 $cm^{-1}$ in 3D-Py-BDA-COF when compared to Py-BDA-COF, which can be attributed to the C═C bond in the conjugated ene-yne unit (Figure S3a).[34−36] These observations unveil the successful polymerization of the BDA moieties within the 3D-Py-BDA-COF. In the spectra of Py-N-COF, Py-BDA-COF, and 3D-Py-BDA-COF, the peak at around 1620 $cm^{-1}$ corresponds to the C═N stretching vibration of the imine bond.[37−39] After the postsulfurization treatment, the stretching band associated with the C═N group disappeared, while distinct peaks characteristic of the thiazole linkage (1595, 1308, and 955 $cm^{-1}$) appeared in Py−N−S-COF and 3D-Py-BDA-S-COF. Overlaying the solid-state $^{13}C$ NMR spectra of Py-BDA-COF and 3D-Py-BDA-S-COF reveals clear chemical structural changes. The diacetylene group in Py-BDA-COF is responsible for the peaks at ∼77 and ∼83 ppm, as illustrated in Figure S4. Following sulfur polymerization, one of C≡C peaks (∼77 ppm) disappeared, which corresponds to the alkynyl groups in the newly created enyne-conjugated chain.[26,33−35,40−42] Additionally, the imine carbon in Py-BDA-COF shifts from ∼153 to ∼163 ppm, indicating the formation of thiazole carbon (S−C═N).[43−45] The successful immobilization of sulfur in Py−N−S-COF and 3D-Py-BDA-S-COF was further confirmed by elemental analysis. The observed theoretical values closely matched their corresponding experimental results (Table S3).

In fact, another possibility arises from the highly active nature of the diacetylene,[36] which may interact with $S_8$ during heating to form sulfur rings or chains. However, no characteristic peaks (S−S: 508 $cm^{-1}$, −SH: 2662 $cm^{-1}$) were observed in the FT-IR spectrum (Figure S5),[31,46] ruling out this possibility in our heating process. Therefore, we hypothesize that in the one-pot system, the BDA moieties in Py-BDA-COF first undergo interlayer polymerization to form 3D-Py-BDA-COF. Whereafter, $S_8$ decomposes into small sulfur molecules, which subsequently attack imines to form thiazole rings. To substantiate this assumption, we performed a two-step synthesis: first, 3D-Py-BDA-COF was synthesized, followed by the addition of $S_8$ under the same heating conditions, yielding 3D-Py-BDA-S-COF-1 (Scheme 1). FT-IR and PXRD results showed that the materials from the two-step and one-pot syntheses were highly consistent and retained high crystallinity (Figure S6).

The surface area and permanent porosity of Py-N-COF, Py−N−S-COF, Py-BDA-COF, 3D-Py-BDA-COF, and 3D-Py-BDA-S-COF were evaluated by $N_2$ adsorption−desorption analysis at 77 K. As depicted in Figure S7, both Py-N-COF and Py−N−S-COF showed a surge in $N_2$ adsorption at the low pressures, followed by a gradual increase as the pressure rises, which is consistent with the characteristics of mesopores. Similarly, Py-BDA-COF, 3D-Py-BDA-COF, and 3D-Py-BDA-S-COF also display type-IV isotherms indicative of mesoporous features (Figures 3b and S8). Furthermore, a significant decrease in the Brunauer−Emmett−Teller (BET) surface area ($S_{BET}$) was noted after the postsulfurization process. The $S_{BET}$ values of Py-N-COF, Py−N−S-COF, Py-BDA-COF, 3D-Py-BDA-COF, and 3D-Py-BDA-S-COF were analyzed to be 1788, 1027, 987, 745, and 650 $m^2/g$, respectively (Figures 3b, S7, S8 and Table 1). The quenched solid density functional theory (QSDFT) model based on nitrogen adsorption branch kernel was used to determine the main pore size distribution, and the results showed that the experimental pore size distributions for Py-N-COF, Py−N−S-COF, Py-BDA-COF, 3D-Py-BDA-COF, and 3D-Py-BDA-S-COF were centered at 2.43, 2.02, 3.25, 2.71, and 2.68 nm, respectively (Figures S9, S10 and Table 1).


https://doi.org/10.1021/jacs.4c15825
J. Am. Chem. Soc. XXXX, XXX, XXX−XXX

**Table 1. Summary of the Properties of the Synthesized COFs**

| COFs | bond type | BET ($m^2/g$) | pore size (nm) | CB (V) | VB (V) | band gap (eV) |
|---|---|---|---|---|---|---|
| | | 2D COFs | | | | |
| Py-N | imine | 1788 | 2.43 | −0.53 | +1.67 | 2.20 |
| Py−N-S | thiazole | 1027 | 2.02 | −0.88 | +0.82 | 1.70 |
| Py-BDA | imine | 987 | 3.25 | −0.41 | +1.93 | 2.34 |
| | | 3D COFs | | | | |
| 3D-Py-BDA | imine | 745 | 2.71 | −0.55 | +1.58 | 2.13 |
| 3D-Py-BDA-S | thiazole | 650 | 2.68 | −0.64 | +1.26 | 1.90 |

Furthermore, X-ray photoelectron spectroscopy (XPS) was applied to verify structural transformations in the COFs. For Py−N−S-COF and 3D-Py-BDA-S-COF, the presence of sulfur is observed in the full survey XPS spectra (Figure S11a,b). The peaks at ∼284.16 and ∼284.49 eV, deconvoluted from the C 1s in Py−N−S-COF and 3D-Py-BDA-S-COF respectively, were assigned to the C−S bond (Figures S12b and 3c). Another proof of the thiazole formation comes from comparing the high-resolution XPS spectra of N 1s before and after sulfurization. In the N 1s spectrum of Py−N−S-COF and 3D-Py-BDA-S-COF, a distinct binding energy peak at ∼400.81 eV indicated the presence of the N═C−S bond (Figures S12d and S13c). These peaks collectively suggest the successful conversion of imine bonds to thiazole bonds in Py−N−S-COF and 3D-Py-BDA-S-COF. Regarding the *z*-axis connectors, the sp (C≡C) signal at ∼285.35 eV from the BDA linker[35,40] was found in C 1s of Py-BDA-COF. In contrast, in 3D-Py-BDA-COF and 3D-Py-BDA-S-COF, the absence of sp (C≡C) hybridized carbons and the new presence of sp (C≡C)/$sp^2$ (C═C) at 285.14 and 285.22 eV respectively, imply the successful conversion from (C≡C) bonds to ethylene bands (Figure 3c).

The above characterization results unambiguously confirm the successful creation of the completely conjugated framework in 3D-Py-BDA-S-COF via a one-pot sulfurization process. The formed 3D thiazole COFs were found to be extremely stable, with the PXRD patterns revealing that 3D-Py-BDA-S-COF still maintains high crystallinity even after 1 day of immersion in 12 M HCl or 14 M NaOH (Figure S14). Thermogravimetric analysis (TGA) was conducted to assess the thermal stability of the COFs after sulfurization, and the results indicated stability up to approximately 400 °C under a nitrogen atmosphere (Figure S15).

Next, the morphologies of Py-BDA-COF before and after post-treatment were analyzed by using field-emission scanning electron microscopy (FE-SEM) and high-resolution transmission electron microscopy (HR-TEM). As illustrated in Figures 3d,f and S16, the SEM images suggest that all materials exhibit similar and relatively regularly stacked chunk morphologies. Meanwhile, the energy dispersive spectrum (EDS) reveals that the elements of 3D-BDA-S-COF are uniformly distributed over the surface (Figure S17). The long-range ordered structures were further visualized by HR-TEM. From Figures 3e,g and S18, despite alterations to both the plane and interlayer structures of Py-BDA-COF, the high crystallinity is clearly retained in the 3D-Py-BDA-S-COF. Also, the unit cell of 3D-Py-BDA-S-COF shrank a little compared to its pristine Py-BDA-COF, which is consistent with the calculation results of cell parameters based on TEM images and PXRD. More specifically, the lattice fringes distances of the Py-BDA-COF and 3D-Py-BDA-S-COF have been determined to 1.609 and 1.523 nm, which were closely related to their (220) crystal plane of the simulated models appearing at $2\theta$ = 5.496 and 5.772° (1.607 and 1.529 nm), respectively.

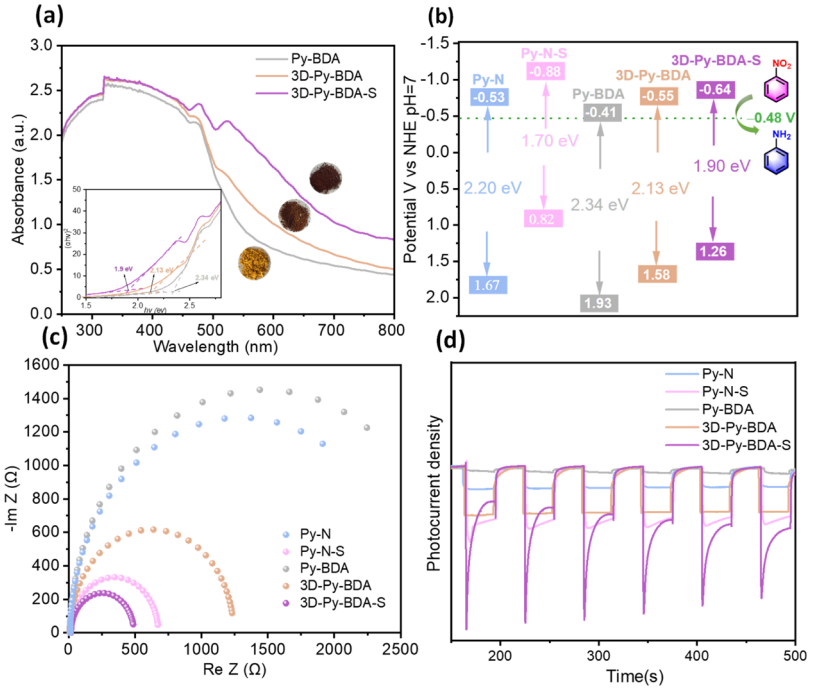


**Figure 4.** (a) UV−vis spectra of Py-BDA-COF, 3D-Py-BDA-COF, and 3D-Py-BDA-S-COF (Inset: Tauc plot), (b) band alignment, (c) electrochemical impedance spectra (EIS), and (d) photocurrent responses of Py-N-COF, Py−N−S-COF, Py-BDA-COF, 3D-Py-BDA-COF, and 3D-Py-BDA-S-COF, respectively.


https://doi.org/10.1021/jacs.4c15825
J. Am. Chem. Soc. XXXX, XXX, XXX−XXX

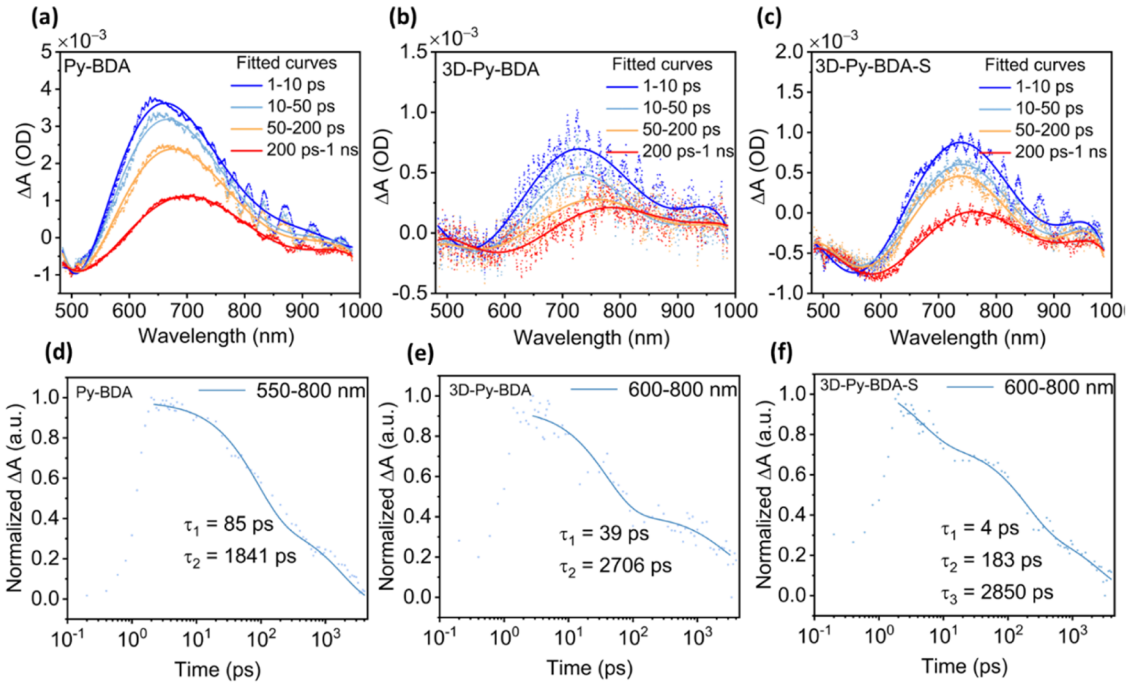


**Figure 5.** Ultrafast fs-TA response of (a) Py-BDA-COF, (b) 3D-Py-BDA-COF, and (c) 3D-Py-BDA-S-COF with corresponding decay profiles at (d) 550−800 nm, (e) 600−800 nm, and (f) 600−800 nm wavelength, respectively.

Moreover, the optoelectronic features of the synthesized COFs were investigated. The solid-state ultraviolet−visible (UV−vis) spectra show that all of the synthesized COFs absorb light in the visible light region (Figures 4a and S19). The 3D-COFs, 3D-Py-BDA-S-COF and 3D-Py-BDA-COF, exhibit stronger absorption in the visible light spectrum than the 2D Py-BDA-COF. This observation highlights the advantages of extended conjugated structures. Using Tauc plot analysis, the optical band gaps ($E_g$) of Py−N−S-COF, 3D-Py-BDA-COF, and 3D-Py-BDA-S-COF were calculated to be 1.70, 2.13, and 1.9 eV, respectively, which are narrower than that of their corresponding Py-N-COF and Py-BDA-COF (2.20 and 2.34 eV) (Table 1). This is due to the enhanced electron delocalization and extended conjugation in Py−N−S-COF, 3D-Py-BDA-COF, and 3D-Py-BDA-S-COF, enhancing regularity within the molecular backbone and resulting in higher electron conductivity. The flat band position ($E_{fb}$) values of these COFs were derived by Mott−Schottky curves at different frequencies (1000, 2000, and 3000 Hz) at their corresponding isoelectric points (Figure S20). Accordingly, the $E_{fb}$ values of Py-N-COF, Py−N−S-COF, Py-BDA-COF, 3D-Py-BDA-COF, and 3D-Py-BDA-S-COF were fitted to be −0.73, −1.08, −0.61, −0.75, and −0.84 V vs Ag/AgCl, respectively. Hence, the $E_{CB}$ for the corresponding COFs, when referenced to standard hydrogen electrodes, were calculated to be −0.53, −0.88, −0.41, −0.55, and −0.64 V vs NHE, respectively (Table 1). Based on the equation $E_{CB} = E_{VB} - E_g$, the valence band ($E_{VB}$) potentials of the COFs were calculated to be +1.67, +0.82, +1.93, +1.58, and +1.26 V vs. NHE, respectively (Figure 4b).

Next, the photocarrier transfer and charge separation resistance were assessed through electrochemical impedance spectroscopy (EIS), transient photocurrent, and photoluminescence tests. In Figure 4c, 3D-Py-BDA-S-COF showed the minimal capacitance arc radius after fitting all of the samples into Nyquist curves, implying the fast transport of photogenerated carriers. The $R_{CT}$ values of each COF are shown in Table S4. Likewise, Py−N−S-COF and 3D-Py-BDA-COF exhibited smaller charge transfer resistances than their pristine Py-N-COF and Py-BDA-COF, suggesting that alterations in the planar or interlayer structures of COFs could influence the interfacial charge transfer rate. As seen in Figures 4d and S21, 3D-Py-BDA-S-COF demonstrated the largest transient-photocurrent response through multiple rounds of on−off photocurrent testing and the lowest emission peak intensity ($\lambda_{ex}$ = 370 nm), potentially indicating more effective charge separation of photogenerated excitons under visible light irradiation. The PL decay lifetime traces further indicate that the 3D-Py-BDA-S-COF possesses longer photocarrier lifetimes (Figure S22). These observations could be primarily attributed to the strong conjugation effect between both the interlayers and the planes in 3D-Py-BDA-S-COF.

To further corroborate our findings, we conducted ultrafast transient absorption spectroscopy. As shown in previous reports,[47] this method measures the change in absorbance $\Delta A$ as a function of wavelength and time after photoexcitation, an approach which allows us to track charge carriers on much shorter time scales after photoexcitation compared to the fluorescence techniques used above. The Py-BDA-COF, 3D-Py-BDA-COF, and 3D-Py-BDA-S-COF were analyzed to obtain a systematic understanding of the transient photoresponse of the COFs incurred by postsynthesis modification (PSM). When excited with a short 170 femtosecond (fs) pump pulse at 343 nm, all three materials showed strong photoinduced or excited state (ESA) absorption features in the 500−750 nm probe window (Figures 5a−c and S23). Two interesting trends can be deduced from the ESA profiles; (1) with gradual structural modifications from 2D to 3D to more conjugated S-containing 3D, the ESA spectrum peak significantly red-shifts, and (2) the decay dynamics of the ESA also changed noticeably during 2D to 3D structural transition. The ESA apexed at *ca.* 650 nm in 2D Py-BDA-COF,


https://doi.org/10.1021/jacs.4c15825
J. Am. Chem. Soc. XXXX, XXX, XXX−XXX

which red-shifted to 730 nm in 3D-Py-BDA-COF, and further to 750 nm for 3D-Py-BDA-S-COF. As ESA features in COFs can most likely be ascribed to higher $S_1 \rightarrow S_n$ transitions, this red-shift signifies that the energy gap between the excited states decreased during 2D-to-3D transition. This observation can be justified by considering the augmented extended conjugation inflicted by the structural changes of the COFs. We conject that the 3D-Py-BDA-S-COF features enhanced electronic delocalization more than the 3D-Py-BDA-COF, which again showed better delocalization than the pristine 2D COF, thereby demonstrating the observed red-shift of ESA.

On the other hand, the change in ESA decay dynamics can be noted where the Py-BDA-COF and 3D-Py-BDA-COF decayed in biexponential pathway (Figure 5d,e) while 3D-Py-BDA-S-COF decayed via a three-exponential model, implying three relaxation pathways (Figure 5f). In 2D COF, two sequential decays with $\tau_1 = 85$ and $\tau_2 = 1841$ ps time constants were recorded, whereas in 3D-Py-BDA-COF, the decay time changed to $\tau_1 = 39$ and $\tau_2 = 2706$ ps. For 3D-Py-BDA-S-COF, by the structural transition from imine to thiazole, the fast 39 ps time scale extends significantly to 183 ps, yet a shorter decay component of 4 ps appears. The latter appearing only in the thiazole linkage is most likely also due to defect trapping at sites that do not present in the imine-based COFs.[48−50] Thus, $\tau_2 = 183$ ps and the slowest pathway ($\tau_3 = 2850$ ps) correspond to $\tau_1$ and $\tau_2$ in Py-BDA-COF and 3D-Py-BDA-COF, respectively, which could be explained by the electron diffusion and recombination of electrons with trapped holes. A longer $\tau_2$ indicates an increased potential for active electron utilization and transfer to other trapping sites. Furthermore, extended dissipation within shallow traps promotes electron activity, contributing to enhanced photocatalytic efficiency.[51,52] In brief, compared to the 2D COF, the 3D-Py-BDA-S-COF exhibits enhanced charge separation, allowing more active electrons to participate in photoreduction reactions, which, in turn, favors the enhancement of photocatalytic activity. Thus, the change in decay profile suggests a change in the generic structure of the material, which further endorses the skeletal change during the 2D imine-to-3D thiazole transition of the COF structures.

**Photoreduction of Nitrobenzene.** The photocatalytic reduction of nitroaromatic compounds to synthesize amines is of great significance, given that amines are pivotal constituents in many chemical processes.[53−55] However, most catalysts for this reduction involve metals or require elevated temperatures.[56] Designing efficient photocatalysts for visible light-driven selective reduction of nitro compounds is an important challenge. On this premise, the photocatalytic activity of the synthesized COFs was evaluated in the photoreduction of nitroaromatic compounds to anilines, with the reduction of nitrobenzene to aniline serving as the model reaction. In this process, hydrazine hydrate served as a hydrogen donor, yielding nontoxic $N_2$ and $H_2O$ as byproducts. Additionally, ethanol was employed as an environmentally friendly solvent, coupled with its role as a sacrificial electron donor (the oxidation potential of $CH_3CH_2OH/CH_3CHO = -0.25$ V vs NHE at pH 7), which facilitates the progression of the photocatalysis process. Initially, the photocatalytic performance of the synthesized COFs for the reduction of nitrobenzene was evaluated at room temperature under 300 W Xe lamp irradiation (light intensity on sample = 42 mW $cm^{-2}$) (Table 2). The 2D imine-linked Py-N-COF and Py-BDA-COF showed negligible catalytic activity in the photoreduction of

**Table 2. Photocatalytic Reduction of Nitrobenzene by Various COFs under Different Reaction Conditions[a]**

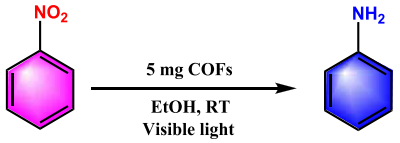


| entry | photocatalyst | time (h) | $N_2H_4{\cdot}H_2O$ (equiv) | conv./sel. (%) |
|---|---|---|---|---|
| 1 | Py-N | 3 | 5 | 3 |
| 2 | Py-BDA | 3 | 5 | 2 |
| 3 | Py−N-S | 3 | 5 | 83/>99 |
| 4 | 3D-Py-BDA | 3 | 5 | 22/>99 |
| 5 | 3D-Py-BDA-S | 3 | 5 | >99/>99 |
| 6 | 3D-Py-BDA-S | 3 | 0 | trace |
| 7[b] | 3D-Py-BDA-S | 3 | 0 | trace |
| 8[c] | 3D-Py-BDA-S | 3 | 0 | 20/>99 |
| 9[d] | 3D-Py-BDA-S | 3 | 5 | trace |
| 10 | no photocatalyst | 3 | 5 | trace |
| 11[e] | 3D-Py-BDA-S | 12 | 5 | >99/>99 |
| 12[f] | 3D-Py-BDA-S | 3 | 5 | 45/>99 |
| 13[g] | 3D-Py-BDA-S | 3 | 5 | 38/>99 |

[a]Standard conditions: substrate 0.1 mmol, 5 mg of COFs, ETOH 1 mL, $N_2H_4{\cdot}H_2O$ (0.5 mmol), Ar (1 atm), 300 W Xe lamp, rt, 3 h, dodecane as an internal standard. [b]Using $H_2$ (balloon) as hydrogen donor. [c]Using $NaBH_4$ as hydrogen donor. [d]Without light irradiation. [e]White LED lamps (15 W). [f]Using $AgNO_3$ as an electron scavenger. [g]Replacing EtOH with acetonitrile (ACN).

nitrobenzene (Table 2, entries 1 and 2). In contrast, the 2D thiazole-linked Py−N−S-COF with extended planar conjugation achieved an 83% conversion of nitrobenzene to aniline within 3 h (Table 2, entry 3). Then, 3D-Py-BDA-COF, with the interlayer conjugation in the *z*-direction but without the thiazole units, exhibits a nitrobenzene conversion of 22% (Table 2, entry 4). The 3D-Py-BDA-S-COF with full conjugation in all 3 dimensions achieves full conversion of nitrobenzene (>99%) (Table 2, entry 5). Here, we emphasize that the CB position of Py-BDA-COF is −0.41 V, which is more positive than the reduction potential of nitrobenzene (−0.48 V) (Figure 4).[53,57] As a result, this reduction process is thermodynamically impossible over Py-BDA-COF. However, after structural modification, the reduction ability of 3D-Py-BDA-S-COF, characterized by a CB of −0.64 V, was significantly enhanced along with an improved charge transfer capability. This enhancement resulted in exceptionally high photoactivity for 3D-Py-BDA-S-COF. The tendency toward photocatalytic ability of these COFs is consistent with these findings.

Next, we tested different reducing agents (hydrogen sources) for the reduction of nitrobenzene using 3D-Py-BDA-S-COF as the photocatalyst. Only trace aniline was detected when $N_2H_4{\cdot}H_2O$ was absent or $H_2$ was used as a hydrogen source (Table 2, entries 6, 7). Additionally, using $NaBH_4$ instead of $N_2H_4{\cdot}H_2O$ led to a significantly reduced nitrobenzene conversion for 3D-Py-BDA-S-COF (20 vs 99%) (Table 2, entry 8). Furthermore, in the absence of a light source or photocatalysts, almost no aniline was detected, indicating that this is a photocatalytic process (Table 2, entries 9−10). Even when we replaced the 300 W Xe light with a lower energy-consuming light source (15 W White LED lamp), still full conversion (>99%) from nitrobenzene to aniline was obtained within 12 h of radiation (Table 2, entry 11). In Table


https://doi.org/10.1021/jacs.4c15825
J. Am. Chem. Soc. XXXX, XXX, XXX−XXX

2, entries 12 and 13, the conversion was significantly reduced when $AgNO_3$ ($e^-$ scavenger) was added to the photocatalytic reaction or when the hole scavenger EtOH was replaced with a redox-stable organic solvent (ACN), emphasizing the pivotal roles of photogenerated electrons and holes in the reduction of nitrobenzene to aniline.

Following the excellent performance of 3D-Py-BDA-S-COF in the reduction reaction of nitrobenzene, a series of nitroaromatic compounds was explored. As summarized in Table S5, all examined nitroaromatic compounds could be completely converted (>99%) to their respective aniline products within 3−4 h. Besides, compared with the other catalysts for light-driven nitrobenzene reduction, 3D-Py-BDA-S COF performed best among the metal-free photocatalysts, mostly due to its highly conjugated structure (Table S6).

**Proposed Mechanism of Nitrobenzene Reduction.** There are currently two potential pathways described in literature for the photocatalytic reduction of nitrobenzene to aniline.[53,58] As depicted in Figure 6a, nitrobenzene (denoted by **A**) can be directly reduced to aniline (denoted by **D**) or undergo a condensation reaction with nitrosobenzene (denoted by **B**) and phenylhydroxylamine (denoted by **C**), resulting in azobenzene (denoted by **E**) which subsequently yields aniline. In order to explore which mechanism prevails in this particular system, we applied GC-MS to monitor the intermediates. First, (**B**) and (**C**) were detected, indicating their involvement in the production of aniline (Figure S24). To further determine the reaction pathway, (**E**), a compound exclusive in Pathway 2, was used as the substrate instead of (**A**). The results showed a negligible amount of (**D**), suggesting that Pathway 2 is not active in our photocatalytic system. As mentioned above, ethanol acts as a hole scavenger. We also wondered whether it could serve as a hydrogen donor in the production of aniline. Therefore, we performed a series of reactions without hydrazine hydrate. As is shown in Table S7 Entry 2, only trace aniline was detected after 3 h. Even with ethanol adjusted to pH 5 using diluted HCl to enhance the hydrogen supply for the reduction of nitrobenzene, a low yield of aniline (8%) was obtained (Table S7 Entry 3). We further calculated the yields of **B** and **C** in the absence of $N_2H_4{\cdot}H_2O$, finding that the predominant product was **C**, with yields of 63−65%, while the yield of **B** was 9−12% (Table S7, Entries 2 and 3). Herein, we infer that ethanol provides a hydrogen source for the reduction of **A** to **C**, which is a photocatalytic process. Indeed, ethanol provides some protons but insufficient hydrogen for efficient nitrobenzene reduction, leading to low aniline yield. To verify this hypothesis, **C** was utilized as a substrate with $N_2H_4{\cdot}H_2O$ as the hydrogen source under identical conditions, yielding aniline at 85% even in the dark after 2 h (Table S7 Entry 4). Thus, the above experiments collectively suggested that ethanol primarily acts as a hole scavenger to prevent recombination and partially aids nitrobenzene reduction, while $N_2H_4{\cdot}H_2O$ supplies sufficient hydrogen, especially for converting **C** to aniline.

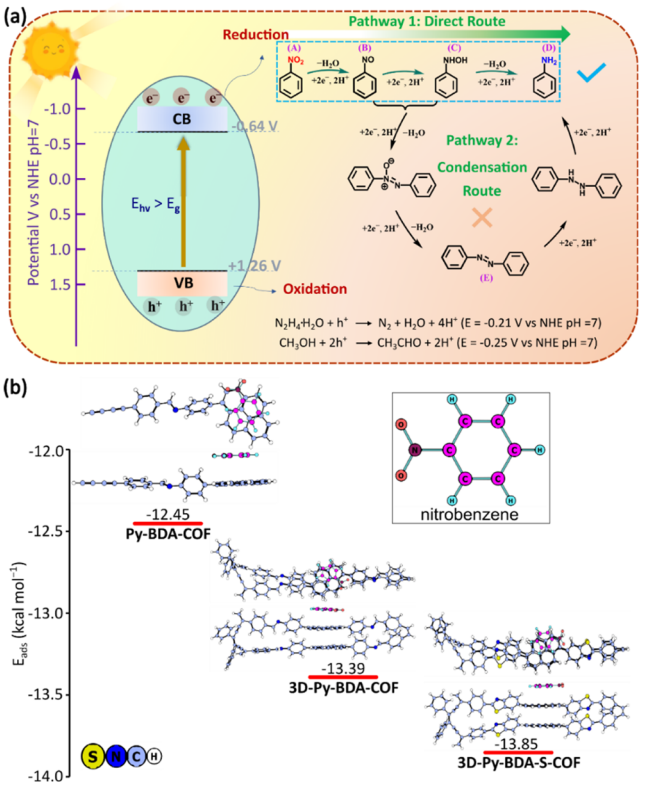


**Figure 6.** (a) Possible mechanisms of the 3D-Py-BDA-S-COF for the reduction of nitrobenzene to aniline. (b) Calculated adsorption energies and optimized geometries (top and side views) of nitrobenzene on Py-BDA-COF, 3D-Py-BDA-COF, and 3D-Py-BDA-S-COF. The lower adsorption energy (far away from zero) denotes stronger adsorption. The atom colors are elaborated in the figure.

Based on the above analysis, a possible mechanism for the photocatalytic reduction of nitrobenzene in the visible light range is illustrated in Figure 6a. When illuminated by visible light, the 3D-Py-BDA-S-COF generates photogenerated electron−hole pairs. The holes, produced at the VB of the COF, rapidly oxidize $N_2H_4{\cdot}H_2O$, resulting in the formation of $N_2$, $H_2O$, and $H^+$, while ethanol also consumed holes and reacted to produce acetaldehyde and $H^+$. Concurrently, the photoinduced electrons on the CB of 3D-Py-BDA-S-COF efficiently participate in the reduction reaction. Nitrobenzene undergoes a stepwise reduction process, initially converting to nitrosobenzene and subsequently to phenylhydroxylamine, ultimately yielding aniline.

Density functional theory (DFT) calculations were employed to explore the adsorption behavior nitrobenzene on different COFs, using the CPCM (ethanol)/B3LYP-D3(BJ)/6-31+G* level of theory.[59−62] Further computational details are provided in the Supporting Information. Various adsorption sites were examined for the Py-BDA-COF, and our calculated adsorption energies ($E_{ads}$) reveal that nitrobenzene adsorbs more strongly to the pyrene moiety (−12.45 kcal mol$^{-1}$) than to other sites (Figure S25). Consequently, only the pyrene moiety was considered for further adsorption investigations. As depicted in Figure 6b, the 2D imine-linked Py-BDA COF exhibits an adsorption energy of −12.45 kcal mol$^{-1}$, indicating a relatively weak interaction with nitrobenzene compared to other COFs. In contrast, after polymerization of the BDA monomer, the 3D-Py-BDA-COF shows an enhanced adsorption energy of −13.39 kcal mol$^{-1}$, suggesting that polymerization along the *z*-axis strengthens the interaction of the COF with nitrobenzene. Notably, converting the imine linkages to thiazole linkages in the 3D-Py-BDA-S-COF results in the highest adsorption energy of −13.85 kcal mol$^{-1}$, attributed to a more fully conjugated system. A similar trend is observed in another 2D COF system, as shown in Figure S26, where the 2D imine-linked Py-N-COF has lower adsorption energy for nitrobenzene compared to the 2D thiazole-linked


https://doi.org/10.1021/jacs.4c15825
J. Am. Chem. Soc. XXXX, XXX, XXX−XXX

Py−N−S-COF, highlighting the role of planar conjugation in enhancing interaction. Based on DFT calculations and experimental data, we propose that the thiazole linkages in 3D-Py-BDA-S-COF enhance nitrobenzene adsorption, while polymerization along the *z*-axis provides additional pathways for charge transfer.

Finally, we studied the recyclability of the 3D-Py-BDA-S-COF. For this purpose, the 3D-Py-BDA-S-COF was recycled via filtration and then subjected to sequential washing with ethanol and acetone repeatedly. We need to caution that recycling experiments should not be conducted when the catalyst has reached complete conversion, as this may obscure the onset of deactivation. A conversion around 50% is ideal for recyclability tests.[63,64] Therefore, in our study, we first monitored the conversion rate of the photocatalytic reaction over time and filtered the photocatalyst after a time that corresponds to around 50% conversion, which was 1 h (Figure S27). The recovered 3D-Py-BDA-S-COF was dried under vacuum and reused in following cycle under same conditions. As shown in Figure S28, the 3D-Py-BDA-S-COF showed good reusability after 5 runs. It is noteworthy that the selectivity of nitrobenzene was maintained at 100% in every recycling experiment. The FT-IR and PXRD patterns of the spent 3D-Py-BDA-S-COF, compared with those of the fresh one (Figures S29 and S30), displayed no noticeable difference after usage. XPS analysis was conducted to evaluate the elemental differences before and after the photocatalytic reaction. The findings revealed negligible changes in the binding energies of the primary peaks (S 2p, C 1s, N 1s, and O 1s), and the S content remained stable at approximately 14% before and after cycling (Figure S31). Moreover, SEM characterization confirms that the morphology of 3D-Py-BDA-S-COF remains unchanged after recycling experiments (Figure S32). All of these results imply the excellent activity and stability of 3D-Py-BDA-S-COF in the photocatalytic reduction of nitrobenzene to aniline. We tested the materials in photocatalytic $H_2O_2$ production and found that Py-BDA-COF, 3D-Py-BDA-COF, and 3D-Py-BDA-S-COF achieved $H_2O_2$ generation rates of 296, 428, and 1345 $\mu$mol $g^{-1}$ $h^{-1}$, respectively. This trend further confirms that enhanced conjugation boosts the photocatalytic activity, which is in line with our observations from the nitrobenzene reduction experiments.

## CONCLUSIONS

In summary, we have successfully constructed a novel fully conjugated 3D-Py-BDA-S-COF via a one-pot sulfurization process. In the planar direction, the pristine 2D imine-linked Py-BDA-COF transformed to a highly conjugated thiazole-linked structure. Meanwhile, solid-state thermal polymerization of BDA moieties in the interlayer direction led to the conversion of diacetylene bands (−C≡C−C≡C−) to −C≡C−C═C− bonds, resulting in the alternating presence of double and triple bonds in the *z*-direction. This achievement enables the transformation from a 2D layered COF (Py-BDA-COF) to a fully conjugated 3D COF (3D-Py-BDA-S-COF). Despite the cyclization of thiazole bonds and the thermal polymerization process, 3D-Py-BDA-S-COF maintains a high crystallinity of the framework. This fully conjugated COF exhibits significantly enhanced photoelectronic properties, achieving nearly complete conversion in the photocatalytic reduction of nitrobenzene. These benefit from the fact that the fully conjugated structure provides more paths for photogenerated carriers and improves the separation efficiency of photogenerated electrons and holes and the lifetime of photogenerated carriers, as shown by electrochemical characterization, PL measurements, and ultrafast TA spectroscopy. These easily synthesized 3D fully conjugated COFs are excellent and stable photoactive materials for a whole range of applications, including photocatalysis, light emission, and sensing.

## ASSOCIATED CONTENT

### Supporting Information

The Supporting Information is available free of charge at https://pubs.acs.org/doi/10.1021/jacs.4c15825.

Experimental procedures and characterization data; materials synthesis and general protocols; additional figures; PXRD patterns; FTIR; TGA; liquid and solid-state NMR spectra; $N_2$ sorption isotherms; pore size distribution plots; XPS; SEM and TEM images; UV−vis studies; fluorescence studies; stability tests; unit cell parameters; DFT calculations; photocatalytic experiment results (PDF)

Final coordinates of atoms in all of the relevant structures for adsorption energy calculations (ZIP)

## AUTHOR INFORMATION


### Corresponding Authors

**Xiao Feng** − *School of Chemistry, Dalian University of Technology, Dalian 116024, P. R. China;* orcid.org/0000-0002-3055-0172; Email: xiaof@dlut.edu.cn.

**Pascal Van Der Voort** − *COMOC-Center for Ordered Materials, Organometallics and Catalysis, Department of Chemistry, Ghent University, 9000 Ghent, Belgium;* orcid.org/0000-0002-1248-479X; Email: pascal.vandervoort@ugent.be

### Authors

**Maojun Deng** − *COMOC-Center for Ordered Materials, Organometallics and Catalysis, Department of Chemistry, Ghent University, 9000 Ghent, Belgium*

**Jeet Chakraborty** − *COMOC-Center for Ordered Materials, Organometallics and Catalysis, Department of Chemistry, Ghent University, 9000 Ghent, Belgium*

**Guizhen Wang** − *Center for Advanced Studies in Precision Instruments, Hainan University, Haikou, Hainan 570228, P. R. China*

**Kuber Singh Rawat** − *Center for Molecular Modeling (CMM), Ghent University, 9052 Zwijnaarde, Belgium*

**Laurens Bourda** − *COMOC-Center for Ordered Materials, Organometallics and Catalysis, Department of Chemistry, Ghent University, 9000 Ghent, Belgium; XStruct, Department of Chemistry, Ghent University, 9000 Ghent, Belgium;* orcid.org/0000-0003-4221-3154

**Jiamin Sun** − *COMOC-Center for Ordered Materials, Organometallics and Catalysis, Department of Chemistry, Ghent University, 9000 Ghent, Belgium;* orcid.org/0009-0005-9423-9411

**Ipsita Nath** − *COMOC-Center for Ordered Materials, Organometallics and Catalysis, Department of Chemistry, Ghent University, 9000 Ghent, Belgium*

**Yanwei Ji** − *Physics and Chemistry of Nanostructures, Department of Chemistry, Ghent University, 9000 Ghent,*




https://doi.org/10.1021/jacs.4c15825
J. Am. Chem. Soc. XXXX, XXX, XXX−XXX

*Belgium; NOLIMITS Center for Non-Linear Microscopy and Spectroscopy, 9000 Ghent, Belgium*

**Pieter Geiregat** − *Physics and Chemistry of Nanostructures, Department of Chemistry, Ghent University, 9000 Ghent, Belgium; NOLIMITS Center for Non-Linear Microscopy and Spectroscopy, 9000 Ghent, Belgium;* orcid.org/0000-0001-7217-8738

**Veronique Van Speybroeck** − *Center for Molecular Modeling (CMM), Ghent University, 9052 Zwijnaarde, Belgium;* orcid.org/0000-0003-2206-178X

Complete contact information is available at: https://pubs.acs.org/10.1021/jacs.4c15825

### Notes

The authors declare no competing financial interest.

## ■ ACKNOWLEDGMENTS

We thank Prof. Dirk Poelman (UGent) for helping with the Solid-state UV−vis measurements. We also would like to thank Lihong Wu for SEM and TEM testing and analysis. M.J.D. (202107565003), J.M.S. (201906060159), and Y.W.J. (202206280022) acknowledge the financial support from the China Scholarship Council (CSC). X.F. acknowledges the National Natural Science Foundation of China (22311530679, 22101039, 22471027), the State Key Laboratory of Catalysis (2024SKL-A-006), and the Fundamental Research Funds for the Central Universities (DUT24LK004). J.C. acknowledges financial support from UGent (BOF. PDO. 2022.0032.01). P.V.D.V. and I.N. acknowledge the Flemish Research Foundation (FWO Vlaanderen) for financial support via project G020521N, J.M.S. acknowledges the financial support from Ghent University (BOF CSC preference program 01SC0619). P.G. acknowledges support from FWO Vlaanderen (project G0B2921N) and the UGent Core Facility program. K.S.R., V.V.S., and P.V.D.V. acknowledge the research board of UGent (BOF) through a Concerted Research Action (GOA010-17). The computational resources (Stevin Supercomputer Infrastructure) and services used in this work were provided by the VSC (Flemish Supercomputer Center) and funded by the Ghent University, FWO and the Flemish Government-department EWI.

## ■ REFERENCES

(1) Gutzler, R.; Perepichka, D. F. π-Electron Conjugation in Two Dimensions. *J. Am. Chem. Soc.* **2013**, *135* (44), 16585−16594.

(2) Dzieszkowski, K.; Pawlicki, M. Triangularly shaped cyclic defects for the selective boron doping of π-extended systems. *Mater. Chem. Front.* **2022**, *6* (22), 3306−3317.

(3) Roncali, J. Synthetic Principles for Bandgap Control in Linear π-Conjugated Systems. *Chem. Rev.* **1997**, *97* (1), 173−206.

(4) Praxedes, F. R.; Nobre, M. A. L.; Poon, P. S.; Matos, J.; Lanfredi, S. Nanostructured $K_xNa_{1-x}NbO_3$ hollow spheres as potential materials for the photocatalytic treatment of polluted water. *Appl. Catal., B* **2021**, *298*, No. 120502.

(5) Cheng, H.; Cheng, J.; Wang, L.; Xu, H. Reaction Pathways toward Sustainable Photosynthesis of Hydrogen Peroxide by Polymer Photocatalysts. *Chem. Mater.* **2022**, *34* (10), 4259−4273.

(6) Lee, J.-S. M.; Cooper, A. I. Advances in Conjugated Microporous Polymers. *Chem. Rev.* **2020**, *120* (4), 2171−2214.

(7) Li, J.; Shen, P.; Zhao, Z.; Tang, B. Z. Through-Space Conjugation: A Thriving Alternative for Optoelectronic Materials. *CCS Chem.* **2019**, *1* (2), 181−196.

(8) Halder, A.; Ghosh, M.; Khayum, M. A.; Bera, S.; Addicoat, M.; Sasmal, H. S.; Karak, S.; Kurungot, S.; Banerjee, R. Interlayer Hydrogen-Bonded Covalent Organic Frameworks as High-Performance Supercapacitors. *J. Am. Chem. Soc.* **2018**, *140* (35), 10941−10945.

(9) Cheng, Y.-Z.; Ji, W.; Hao, P.-Y.; Qi, X.-H.; Wu, X.; Dou, X.-M.; Bian, X.-Y.; Jiang, D.; Li, F.-T.; Liu, X.-F.; Yang, D.-H.; Ding, X.; Han, B.-H. A Fully Conjugated Covalent Organic Framework with Oxidative and Reductive Sites for Photocatalytic Carbon Dioxide Reduction with Water. *Angew. Chem., Int. Ed.* **2023**, *62* (36), No. e202308523.

(10) Zhao, C.; Chen, Z.; Shi, R.; Yang, X.; Zhang, T. Recent Advances in Conjugated Polymers for Visible-Light-Driven Water Splitting. *Adv. Mater.* **2020**, *32* (28), No. 1907296.

(11) Deng, M.; Sun, J.; Laemont, A.; Liu, C.; Wang, L.; Bourda, L.; Chakraborty, J.; Van Hecke, K.; Morent, R.; De Geyter, N.; Leus, K.; Chen, H.; Van Der Voort, P. Extending the π-conjugation system of covalent organic frameworks for more efficient photocatalytic $H_2O_2$ production. *Green Chem.* **2023**, *25* (8), 3069−3076.

(12) Wang, Y.; Cheng, Y. Z.; Wu, K. M.; Yang, D. H.; Liu, X. F.; Ding, X.; Han, B. H. J. A. C. Linkages make a difference in the photoluminescence of covalent organic frameworks. *Angew. Chem.* **2023**, *135* (42), No. e202310794.

(13) Ren, X.; Liao, G.; Li, Z.; Qiao, H.; Zhang, Y.; Yu, X.; Wang, B.; Tan, H.; Shi, L.; Qi, X.; Zhang, H. Two-dimensional MOF and COF nanosheets for next-generation optoelectronic applications. *Coord. Chem. Rev.* **2021**, *435*, No. 213781.

(14) Li, J.; Jing, X.; Li, Q.; Li, S.; Gao, X.; Feng, X.; Wang, B. Bulk COFs and COF nanosheets for electrochemical energy storage and conversion. *Chem. Soc. Rev.* **2020**, *49* (11), 3565−3604.

(15) Yang, Z.; Liu, J.; Li, Y.; Zhang, G.; Xing, G.; Chen, L. J. A. C. Arylamine-linked 2D covalent organic frameworks for efficient pseudocapacitive energy storage. *Angew. Chem.* **2021**, *133* (38), 20922−20927.

(16) Huang, W.; Zhang, W.; Yang, S.; Wang, L.; Yu, G. 3D Covalent Organic Frameworks from Design, Synthesis to Applications in Optoelectronics. *Small* **2024**, *20* (18), No. 2308019.

(17) Xie, Y.; Wang, W.; Zhang, Z.; Li, J.; Gui, B.; Sun, J.; Yuan, D.; Wang, C. Fine-tuning the pore environment of ultramicroporous three-dimensional covalent organic frameworks for efficient one-step ethylene purification. *Nat. Commun.* **2024**, *15* (1), No. 3008.

(18) Wang, X.; Wada, Y.; Shimada, T.; Kosaka, A.; Adachi, K.; Hashizume, D.; Yazawa, K.; Uekusa, H.; Shoji, Y.; Fukushima, T.; Kawano, M.; Murakami, Y. Triple Isomerism in 3D Covalent Organic Frameworks. *J. Am. Chem. Soc.* **2024**, *146* (3), 1832−1838.

(19) Liu, X.; Wang, Z.; Zhang, Y.; Yang, N.; Gui, B.; Sun, J.; Wang, C. Gas-Triggered Gate-Opening in a Flexible Three-Dimensional Covalent Organic Framework. *J. Am. Chem. Soc.* **2024**, *146* (16), 11411−11417.

(20) Gui, B.; Lin, G.; Ding, H.; Gao, C.; Mal, A.; Wang, C. Three-Dimensional Covalent Organic Frameworks: From Topology Design to Applications. *Acc. Chem. Res.* **2020**, *53* (10), 2225−2234.

(21) Cheng, Y.; Xin, J.; Xiao, L.; Wang, X.; Zhou, X.; Li, D.; Gui, B.; Sun, J.; Wang, C. A Fluorescent Three-Dimensional Covalent Organic Framework Formed by the Entanglement of Two-Dimensional Sheets. *J. Am. Chem. Soc.* **2023**, *145* (34), 18737−18741.

(22) Gui, B.; Xin, J.; Cheng, Y.; Zhang, Y.; Lin, G.; Chen, P.; Ma, J.-X.; Zhou, X.; Sun, J.; Wang, C. Crystallization of Dimensional Isomers in Covalent Organic Frameworks. *J. Am. Chem. Soc.* **2023**, *145* (20), 11276−11281.

(23) Zhu, T.; Kong, Y.; Lyu, B.; Cao, L.; Shi, B.; Wang, X.; Pang, X.; Fan, C.; Yang, C.; Wu, H.; Jiang, Z. 3D covalent organic framework membrane with fast and selective ion transport. *Nat. Commun.* **2023**, *14* (1), No. 5926.

(24) Jadhav, T.; Fang, Y.; Liu, C.-H.; Dadvand, A.; Hamzehpoor, E.; Patterson, W.; Jonderian, A.; Stein, R. S.; Perepichka, D. F. Transformation between 2D and 3D Covalent Organic Frameworks via Reversible [2 + 2] Cycloaddition. *J. Am. Chem. Soc.* **2020**, *142* (19), 8862−8870.

(25) Ding, J.; Guan, X.; Lv, J.; Chen, X.; Zhang, Y.; Li, H.; Zhang, D.; Qiu, S.; Jiang, H.-L.; Fang, Q. Three-Dimensional Covalent

Organic Frameworks with Ultra-Large Pores for Highly Efficient Photocatalysis. *J. Am. Chem. Soc.* **2023**, *145* (5), 3248−3254.
(26) Zhu, Y.; Shao, P.; Hu, L.; Sun, C.; Li, J.; Feng, X.; Wang, B. Construction of Interlayer Conjugated Links in 2D Covalent Organic Frameworks via Topological Polymerization. *J. Am. Chem. Soc.* **2021**, *143* (21), 7897−7902.
(27) Wang, K.; Hou, B.; Dong, J.; Niu, H.; Liu, Y.; Cui, Y. Controlling the Degree of Interpenetration in Chiral Three-Dimensional Covalent Organic Frameworks via Steric Tuning. *J. Am. Chem. Soc.* **2024**, *146* (31), 21466−21475.
(28) Haase, F.; Troschke, E.; Savasci, G.; Banerjee, T.; Duppel, V.; Dörfler, S.; Grundei, M. M. J.; Burow, A. M.; Ochsenfeld, C.; Kaskel, S.; Lotsch, B. V. Topochemical conversion of an imine- into a thiazole-linked covalent organic framework enabling real structure analysis. *Nat. Commun.* **2018**, *9* (1), No. 2600.
(29) Huang, Q.; Wu, W.; Ai, K.; Liu, J. Highly Sensitive Polydiacetylene Ensembles for Biosensing and Bioimaging. *Front. Chem.* **2020**, *8*, No. 565782.
(30) Liang, B.; Zhao, J.; Wang, J.; Li, Y.; Han, B.; Li, J.; Ding, X.; Xie, Z.; Wang, H.; Zhou, S. Nonlinear optical properties of porphyrin-based covalent organic frameworks determined by steric-orientation of conjugation. *J. Mater. Chem. C* **2023**, *11* (9), 3354−3359.
(31) Xu, F.; Yang, S.; Chen, X.; Liu, Q.; Li, H.; Wang, H.; Wei, B.; Jiang, D. Energy-storage covalent organic frameworks: improving performance via engineering polysulfide chains on walls. *Chem. Sci.* **2019**, *10* (23), 6001−6006.
(32) Dhaka, A.; Jeon, I. R.; Jeannin, O.; Aubert, E.; Espinosa, E.; Fourmigué, M. J. A. C. Topochemical Polymerization of a Diacetylene in a Chalcogen-Bonded (ChB) Assembly. *Angew. Chem.* **2022**, *134* (10), No. e202116650.
(33) Kumar, N. R.; Das, P.; Agrawal, A. R.; Mandal, S. K.; Zade, S. S. Thienyltriazine based conjugated porous organic polymers: tuning of the porosity and band gap, and $CO_2$ capture. *Mater. Adv.* **2021**, *2* (22), 7473−7481.
(34) Zhao, Z.; Zheng, Y.; Wang, C.; Zhang, S.; Song, J.; Li, Y.; Ma, S.; Cheng, P.; Zhang, Z.; Chen, Y. Fabrication of Robust Covalent Organic Frameworks for Enhanced Visible-Light-Driven $H_2$ Evolution. *ACS Catal.* **2021**, *11* (4), 2098−2107.
(35) Chen, L.; Wang, L.; Wan, Y.; Zhang, Y.; Qi, Z.; Wu, X.; Xu, H. Acetylene and Diacetylene Functionalized Covalent Triazine Frameworks as Metal-Free Photocatalysts for Hydrogen Peroxide Production: A New Two-Electron Water Oxidation Pathway. *Adv. Mater.* **2020**, *32* (2), No. 1904433.
(36) Dhaka, A.; Jeon, I.-R.; Jeannin, O.; Aubert, E.; Espinosa, E.; Fourmigué, M. Topochemical Polymerization of a Diacetylene in a Chalcogen-Bonded (ChB) Assembly. *Angew. Chem., Int. Ed.* **2022**, *61* (10), No. e202116650.
(37) Li, H.; Zhou, Z.; Ma, T.; Wang, K.; Zhang, H.; Alawadhi, A. H.; Yaghi, O. M. Bonding of Polyethylenimine in Covalent Organic Frameworks for $CO_2$ Capture from Air. *J. Am. Chem. Soc.* **2024**, *146* (51), 35486−35492.
(38) Song, Q.; Yang, J.; Zheng, K.; Zhang, T.; Yuan, C.; Yuan, L.-M.; Hou, X. Chiral Memory in Dynamic Transformation from Porous Organic Cages to Covalent Organic Frameworks for Enantiorecognition Analysis. *J. Am. Chem. Soc.* **2024**, *146* (11), 7594−7604.
(39) Li, W.; Han, S.; Xiao, C.; Yan, J.; Wu, B.; Wen, P.; Lin, J.; Chen, M.; Lin, X. High-Voltage Single-Ion Covalent Organic Framework Electrolytes Enabled by Nitrile Migration Ladders for Lithium Metal Batteries. *Angew. Chem., Int. Ed.* **2024**, *63* (42), No. e202410392.
(40) Wang, L.; Wan, Y.; Ding, Y.; Wu, S.; Zhang, Y.; Zhang, X.; Zhang, G.; Xiong, Y.; Wu, X.; Yang, J.; Xu, H. Conjugated Microporous Polymer Nanosheets for Overall Water Splitting Using Visible Light. *Adv. Mater.* **2017**, *29* (38), No. 1702428.
(41) Pachfule, P.; Acharjya, A.; Roeser, J.; Langenhahn, T.; Schwarze, M.; Schomäcker, R.; Thomas, A.; Schmidt, J. Diacetylene Functionalized Covalent Organic Framework (COF) for Photocatalytic Hydrogen Generation. *J. Am. Chem. Soc.* **2018**, *140* (4), 1423−1427.
(42) Liu, S.; Chen, M.; Zhao, Y.; Xing, G.; Zhu, W.; Ben, T. Topochemical cross-linking of diacetylene in a highly interpenetrated three-dimensional covalent organic framework. *Chem. Commun.* **2024**, *60* (62), 8051−8054.
(43) Paul, R.; Chandra Shit, S.; Mandal, H.; Rabeah, J.; Kashyap, S. S.; Nailwal, Y.; Shinde, D. B.; Lai, Z.; Mondal, J. Benzothiazole-Linked Metal-Free Covalent Organic Framework Nanostructures for Visible-Light-Driven Photocatalytic Conversion of Phenylboronic Acids to Phenols. *ACS Appl. Nano Mater.* **2021**, *4* (11), 11732−11742.
(44) Waller, P. J.; AlFaraj, Y. S.; Diercks, C. S.; Jarenwattananon, N. N.; Yaghi, O. M. Conversion of Imine to Oxazole and Thiazole Linkages in Covalent Organic Frameworks. *J. Am. Chem. Soc.* **2018**, *140* (29), 9099−9103.
(45) Wang, K.; Jia, Z.; Bai, Y.; Wang, X.; Hodgkiss, S. E.; Chen, L.; Chong, S. Y.; Wang, X.; Yang, H.; Xu, Y.; Feng, F.; Ward, J. W.; Cooper, A. I. Synthesis of Stable Thiazole-Linked Covalent Organic Frameworks via a Multicomponent Reaction. *J. Am. Chem. Soc.* **2020**, *142* (25), 11131−11138.
(46) Haldar, S.; Wang, M.; Bhauriyal, P.; Hazra, A.; Khan, A. H.; Bon, V.; Isaacs, M. A.; De, A.; Shupletsov, L.; Boenke, T.; Grothe, J.; Heine, T.; Brunner, E.; Feng, X.; Dong, R.; Schneemann, A.; Kaskel, S. Porous Dithiine-Linked Covalent Organic Framework as a Dynamic Platform for Covalent Polysulfide Anchoring in Lithium−Sulfur Battery Cathodes. *J. Am. Chem. Soc.* **2022**, *144* (20), 9101−9112.
(47) Chakraborty, J.; Chatterjee, A.; Molkens, K.; Nath, I.; Arenas Esteban, D.; Bourda, L.; Watson, G.; Liu, C.; Van Thourhout, D.; Bals, S.; Geiregat, P.; Van der Voort, P. Decoding Excimer Formation in Covalent−Organic Frameworks Induced by Morphology and Ring Torsion. *Adv. Mater.* **2024**, *36* (26), No. 2314056.
(48) Qiu, J.; Meng, K.; Zhang, Y.; Cheng, B.; Zhang, J.; Wang, L.; Yu, J. COF/$In_2S_3$ S-Scheme Photocatalyst with Enhanced Light Absorption and $H_2O_2$-Production Activity and fs-TA Investigation. *Adv. Mater.* **2024**, *36* (24), No. 2400288.
(49) Zhao, Y.; Yang, C.; Zhang, S.; Sun, G.; Zhu, B.; Wang, L.; Zhang, J. Investigating the charge transfer mechanism of ZnSe QD/COF S-scheme photocatalyst for $H_2O_2$ production by using femtosecond transient absorption spectroscopy. *Chin. J. Catal.* **2024**, *63*, 258−269.
(50) Kim, T. W.; Jun, S.; Ha, Y.; Yadav, R. K.; Kumar, A.; Yoo, C.-Y.; Oh, I.; Lim, H.-K.; Shin, J. W.; Ryoo, R.; Kim, H.; Kim, J.; Baeg, J.-O.; Ihee, H. Ultrafast charge transfer coupled with lattice phonons in two-dimensional covalent organic frameworks. *Nat. Commun.* **2019**, *10* (1), No. 1873.
(51) Wang, W.; Bai, X.; Ci, Q.; Du, L.; Ren, X.; Phillips, D. L. Near-Field Drives Long-Lived Shallow Trapping of Polymeric $C_3N_4$ for Efficient Photocatalytic Hydrogen Evolution. *Adv. Funct. Mater.* **2021**, *31* (35), No. 2103978.
(52) Chen, Y.; Cheng, Y.; Liu, Y.; Wang, Y.; Qu, Y.; Jiang, D.; Qin, Z.; Yuan, Y. Achieving long-lived shallow trapping states in carbon nitride through the n-$\pi^*$electronic transition for enhanced photocatalytic hydrogen generation. *Appl. Catal., B* **2024**, *342*, No. 123453.
(53) Jiao, J.; Sun, H.; Si, C.; Xu, J.; Zhang, T.; Han, Q. Photocatalytic Multielectron Reduction of Nitroarenes to Anilines by Utilizing an Electron-Storable Polyoxometalate-Based Metal−Organic Framework. *ACS Appl. Mater. Interfaces* **2022**, *14* (14), 16386−16393.
(54) Xie, Y.; Shang, X.; Liu, D.; Zhao, H.; Gu, Y.; Zhang, Z.; Wang, X. Non-noble metal thickness-tunable $Bi_2MoO_6$ nanosheets for highly efficient visible-light-driven nitrobenzene reduction into aniline. *Appl. Catal., B* **2019**, *259*, No. 118087.
(55) Yuan, Z.; Huang, L.; Liu, Y.; Sun, Y.; Wang, G.; Li, X.; Lercher, J. A.; Zhang, Z. Synergy of Oxygen Vacancies and Base Sites for Transfer Hydrogenation of Nitroarenes on Ceria Nanorods. *Angew. Chem., Int. Ed.* **2024**, *63* (9), No. e202317339.
(56) Abednatanzi, S.; Gohari Derakhshandeh, P.; Dalapati, S.; Veerapandian, S. K. P.; Froissart, A.-C.; Epping, J. D.; Morent, R.; De Geyter, N.; Van Der Voort, P. Metal-Free Chemoselective Reduction of Nitroarenes Catalyzed by Covalent Triazine Frameworks: The Role


https://doi.org/10.1021/jacs.4c15825
J. Am. Chem. Soc. XXXX, XXX, XXX−XXX

of Embedded Heteroatoms. *ACS Appl. Mater. Interfaces* **2022**, *14* (13), 15287−15297.
(57) Anuchai, S.; Juntrapirom, S.; Jarusupakornkul, K.; Tantraviwat, D.; Inceesungvorn, B. Oxygen vacancy-rich BiOBr microflowers for enhancing photocatalytic reduction of nitrobenzene under visible light. *Colloids Surf., A* **2023**, *664*, No. 131102.
(58) Wang, S.; Li, S.; Feng, H.; Yang, W.; Feng, Y.-S. Visible-Light-Driven Porphyrin-Based Bimetallic Metal−Organic Frameworks for Selective Photoreduction of Nitro Compounds under Mild Conditions. *ACS Appl. Mater. Interfaces* **2023**, *15* (3), 4845−4856.
(59) Becke, A. D. Density-functional thermochemistry. I. The effect of the exchange-only gradient correction. *J. Chem. Phys.* **1992**, *96* (3), 2155−2160.
(60) Grimme, S.; Antony, J.; Ehrlich, S.; Krieg, H. A consistent and accurate ab initio parametrization of density functional dispersion correction (DFT-D) for the 94 elements H-Pu. *J. Chem. Phys.* **2010**, *132*, No. 154104.
(61) Grimme, S.; Ehrlich, S.; Goerigk, L. Effect of the damping function in dispersion corrected density functional theory. *J. Comput. Chem.* **2011**, *32* (7), 1456−1465.
(62) Lee, C.; Yang, W.; Parr, R. G. Development of the Colle-Salvetti correlation-energy formula into a functional of the electron density. *Phys. Rev. B* **1988**, *37* (2), 785−789.
(63) Ma, J.; Mao, X.; Hu, C.; Wang, X.; Gong, W.; Liu, D.; Long, R.; Du, A.; Zhao, H.; Xiong, Y. Highly Efficient Iron-Based Catalyst for Light-Driven Selective Hydrogenation of Nitroarenes. *J. Am. Chem. Soc.* **2024**, *146* (1), 970−978.
(64) Li, G.; Zheng, S.; Wang, L.; Zhang, X. Metal-Free Chemoselective Hydrogenation of Nitroarenes by N-Doped Carbon Nanotubes via In Situ Polymerization of Pyrrole. *ACS Omega* **2020**, *5* (13), 7519−7528.


https://doi.org/10.1021/jacs.4c15825
*J. Am. Chem. Soc.* XXXX, XXX, XXX−XXX